Analysis and modeling of localized invariant solutions in pipe flow

Paul Ritter,[1,2] Stefan Zammert,[3] Baofang Song,[4,1] Bruno Eckhardt,[5,6] and Marc Avila[1,2,*]

[1] *Center of Applied Space Technology and Microgravity (ZARM), University of Bremen, 28359 Bremen, Germany*
[2] *Institute of Fluid Mechanics, Friedrich-Alexander-Universität Erlangen-Nürnberg, 91058 Erlangen, Germany*
[3] *Laboratory for Aero- and Hydrodynamics, TU Delft, 2682 Delft, The Netherlands*
[4] *Center for Applied Mathematics, Tianjin University, Tianjin 300072, China*
[5] *Fachbereich Physik, Philipps-Universität Marburg, 35032 Marburg, Germany*
[6] *JM Burgerscentrum, TU Delft, 2682 Delft, The Netherlands*

Turbulent spots surrounded by laminar flow are a landmark of transitional shear flows, but the dependence of their kinematic properties on spatial structure is poorly understood. We here investigate this dependence in pipe flow for Reynolds numbers between 1500 and 5000. We compute spatially localized relative periodic orbits in long pipes and show that their upstream and downstream fronts decay exponentially towards the laminar profile. This allows us to model the fronts by employing the linearized Navier–Stokes equations, and the resulting model yields the spatial decay rate and the front velocity profiles of the periodic orbits as a function of Reynolds number, azimuthal wave number and propagation speed. In addition, when applied to a localized turbulent puff, the model is shown to accurately approximate the spatial decay rate of its upstream and downstream tails. Our study provides insight into the relationship between the kinematics and spatial structure of localized turbulence and more generally into the physics of localization.

I. INTRODUCTION

Due to its stochastic and fluctuating nature, the classical approach towards understanding turbulent fluids has been a statistical one, which dates back to Osbourne Reynolds [1]. In recent years an alternative approach has emerged, in which the (discretised) Navier-Stokes equations are viewed as a high-dimensional dynamical system and the tools of bifurcation and chaos theory are applied to describe turbulent motions [2–4]. The key idea of this approach is that the turbulent dynamics is shaped by simple exact invariant solutions to the governing equations such as traveling waves [5, 6] and relative periodic orbits [7, 8] in pipe flow. The dynamically most relevant solutions are mildly unstable so that a generic turbulent trajectory spends a significant amount of time in their vicinity [9–11]. Turbulent trajectories depart from the vicinity of the solutions along their unstable manifolds, which can subsequently govern the flow evolution for a considerable period of time [12]. In principle, all properties of the turbulent flow can be derived by an appropriate weighted average over the fundamental solutions [13–17], but deploying this approach is extremely challenging even at low (transitional) Reynolds numbers [11, 17, 18].

Transitional shear flows are characterized by localized chaotic spots surrounded by laminar flow [19–22]. These spots already contain all the salient features of fully turbulent flow [23–25] and hence pose an ideal prototype for a bottom-up study of turbulent dynamics. Because of prevalence of intermittency at the onset of turbulent shear flow [26–28], spatially localized invariant solutions are indispensable for its successful description as a dynamical system. The first such solutions were discovered in plane Couette flow by Schneider *et al.* [29], who computed spanwise-localized equilibria and traveling waves in wide but streamwise short domains.

The first streamwise-localized simple invariant solution was found by Avila *et al.* in pipe flow [30]. It is a relative periodic orbit with reflectional and two-fold rotational symmetry appearing at a saddle-node bifurcation. In this symmetry subspace the lower branch solution (shown in fig. 1a and referred to as LB_2 in the following) has a single unstable direction, whereas the upper branch solution is stable close to the saddle-node bifurcation. As the Reynolds number increases, a bifurcation cascade culminating at a boundary crisis gives rise to transient chaotic dynamics [30, 31], and subsequent changes in the phase-space progressively enhance the spatio-temporal complexity of the flow [31, 32]. The bifurcations of the coherent structures in pipe flow follow the same pattern as observed in small computational cells in plane Couette [17, 33] and plane Poiseuille flows [34]. The finding of spanwise- and streamwise-localized solutions in both flows [35, 36] suggests that similar scenarios may occur in spatially extended domains.

Gibson and Brand [36] observed that the amplitude of spanwise localized equilibria in Couette flow decays exponentially far enough from their energetic core. Hence they proposed to model their spatial decay by using the linearized Navier–Stokes equations and solving the arising eigenvalue problem. Interestingly, their model gave with high accuracy the observed spatial decay rates and their dependence on streamwise wave number and the Reynolds number. A simplified version of their model was shown by the same authors to accurately reproduce the spatial decay of their doubly-localized solutions in the streamwise direction [37].

Recently, Zammert and Eckhardt [38] and Barnett *et al.* [39] applied similar approaches to streamwise-localized relative periodic orbits in channel flow, where

* Corresponding author: marc.avila@zarm.uni-bremen.de

the decay rates also depend on their group velocity, in addition to the spanwise wave number and the Reynolds number. In this paper, we investigate spatial localization in pipe flow. For this purpose, we compute LB_2 and its three-fold cousin [40] (LB_3, see fig. 1b) for a wide range of Reynolds numbers. As in channel flows, we find that the tails of the states decay exponentially in the streamwise direction and that the decay rates can be deduced from the linearized Navier–Stokes equations. However, pipe flow does not permit the simplified modeling approaches used by Brand and Gibson [37], and Zammert and Eckhardt [38]. Furthermore, we extend the analysis to the upstream and downstream tails of localized turbulent puffs and verify that the correct decay rates are obtained for such chaotically evolving states as well.

II. NUMERICAL METHOD

We consider the incompressible, isothermal flow of a fluid with constant density ρ and kinematic viscosity ν in a cylindrical pipe of radius R driven at a constant average speed $\overline{U}$. This flow is governed by the Navier-Stokes equations (NSE):

$$\frac{\mathrm{D}\boldsymbol{U}}{\mathrm{D}t} = \frac{\partial \boldsymbol{U}}{\partial t} + \boldsymbol{U}\cdot\boldsymbol{\nabla}\boldsymbol{U} = -\frac{1}{\rho}\boldsymbol{\nabla}P + \nu\nabla^2\boldsymbol{U} \tag{1a}$$

$$\boldsymbol{\nabla}\cdot\boldsymbol{U} = \left(\frac{1}{r}+\frac{\partial}{\partial r}\right)U_r + \frac{1}{r}\frac{\partial}{\partial\theta}U_\theta + \frac{\partial}{\partial z}U_z = 0, \tag{1b}$$

where P is the pressure and $\boldsymbol{U} = [U_r, U_\theta, U_z](r,\theta,z,t)$ is the fluid velocity field in cylindrical coordinates. It satisfies the no-slip boundary condition at the pipe wall and periodic boundary conditions in the azimuthal and axial directions. The length of the computational domain was chosen sufficiently large in order to avoid interaction of the two fronts via the axial periodicity. All results shown in this paper were obtained in pipes of $200R$ (LB_2) and $160R$ (LB_3) in length.

The *Hagen-Poiseuille* profile is the steady, parabolic laminar solution and reads (subscript "b" is for *base flow*):

$$\boldsymbol{U}_\mathrm{b} = U_\mathrm{cl}\left[1-\left(\frac{r}{R}\right)^2\right]\hat{\boldsymbol{z}}, \quad U_\mathrm{cl} = 2\,\overline{U}, \tag{2}$$

$$-\boldsymbol{\nabla}P_\mathrm{b} = \Pi_\mathrm{b}\hat{\boldsymbol{z}} = \frac{4\mu U_\mathrm{cl}}{R^2}\,\hat{\boldsymbol{z}}, \tag{3}$$

where U_cl is the maximum velocity at the centerline, and $\hat{\boldsymbol{z}}$ denotes the axial unit vector. To facilitate both numerical and theoretical treatment, the NSE are rendered dimensionless by using U_cl, ρU_cl^2 and R as reference scales for the velocity, pressure and length, respectively. As a consequence, the dimensionless NSE are identical to eq. (1) but setting $\rho = 1$ and replacing the viscosity with the inverse of the Reynolds number $1/\mathrm{Re} = \nu/(U_\mathrm{cl}R)$, which is the sole control parameter of the problem. The velocity and pressure gradient of the dimensionless laminar flow then take the form $(1-r^2)\hat{\boldsymbol{z}}$ and $4/\mathrm{Re}$, respectively. Throughout the paper the velocity disturbance $\boldsymbol{u} = \boldsymbol{U} - \boldsymbol{U}_\mathrm{b}$ is used to visualize the structures.

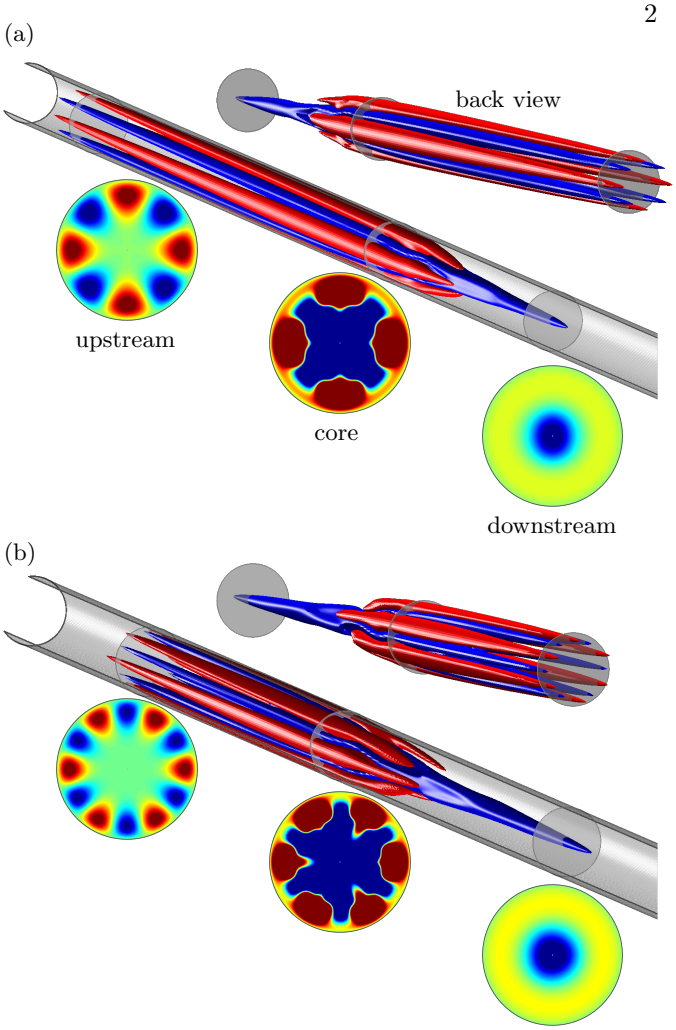

FIG. 1. Structure of the investigated localized reflection-symmetric relative periodic solutions obtained by directly solving the Navier–Stokes equation with a Newton–Krylov method at Re = 3000, (a) twofold (LB_2), (b) threefold (LB_3) rotational symmetry. The central image shows isosurfaces and cross-sections of the streamwise velocity disturbance (*i.e.* with the laminar flow subtracted). Red (blue) streaks are faster (slower) than base flow. In order to highlight the tails of the solutions, the isovalues have been chosen small: $\pm 0.025\,U_\mathrm{cl}$. The axial extent of the shown isosurfaces is about $60R$. The upper right panel shows the upstream front of the same state, which appears shorter due to a different perspective.

The direct numerical simulations of the Navier–Stokes equations (1) have been carried out using openpipeflow.org [41], a hybrid spectral finite-difference Navier-Stokes solver, which uses primitive variables and a PPE-formulation with correct pressure boundary conditions via the influence-matrix method [42, 43]. In order to compute the localized structures, a two-step approach was employed. First, the edge-tracking technique [44, 45] was used to bracket the relative periodic orbits to

a sufficient degree so that it could be converged in a second step with a Newton–Krylov-hookstep algorithm [46] to relative error 10^{-6}. The necessary spatial resolution of the periodic directions depends on the enforced rotational symmetry. We used an axial resolution $-K \dots K$ of ± 768 Fourier modes for a pipe of length $200R$ in case of two-fold symmetry and the same amount of modes for a $160R$ pipe in the three-fold case. The spanwise resolution was ± 12 (± 16) Fourier modes for LB_3 (LB_2) capturing up to 36th (32nd) wave number (of which a third/half has the same amplitude due to symmetry). The code uses the 3/2-rule for dealiasing (*i.e.* padding) resulting in a physical grid which has three times as many points as there are wave numbers K ($3/2 * 2K$). The radial direction has been discretized with a minimum of 48 and maximum of 72 finite-difference nodes depending on Re and pipe length. The time step was fixed at a value of $0.01R/U_{\mathrm{cl}}$.

III. EXPONENTIAL LOCALISATION OF SOLUTIONS

The approach of the fields to the asymptotic parabolic flow is best visualized by the deviation $\boldsymbol{u}$ from the Hagen-Poiseuille profile, since it has to decay to zero. The isosurfaces of streamwise velocity deviation from laminar flow u_z shown in fig. 1 illustrate the spatial arrangement of streaks of the spatially localized relative periodic orbits LB_2 and LB_3 at $\mathrm{Re} = 3000$. Far from the active core, all three velocity components decay quickly with respect to the streamwise direction z. The semilogarithmic representation in fig. 2 shows that the decay is predominantly exponential, with u_z approximately two orders of magnitude larger than the cross-stream velocities u_r and u_θ, thus dominating the decay toward laminar flow. Interestingly, the decay rate of the azimuthal velocity at the downstream tail differs from that of the other two components. To shed light on the origin of this difference, isosurfaces of all three velocity components are shown in fig. 3 for LB_3. In the upstream tail all three velocity components feature a predominant sixfold rotational symmetry, whereas in the downstream tail u_r and u_z are predominantly axisymmetric and u_θ features a threefold symmetric structure. LB_2 exhibits the same features but with fourfold and twofold symmetry, instead of sixfold and threefold, respectively, and hence it is not shown here.

The length of the core of LB_2 and LB_3 remains nearly constant, whereas its amplitude decreases as Re increases (see fig. 4). This is not surprising because LB_2 and LB_3 are edge states and can thus be seen as minimal seeds to trigger turbulence [47]. The decay rate of both their upstream and downstream tails decreases with Re, *i.e.* the axial velocity profile gradually "opens up". There is a marked asymmetry, however. While the decay rates of the downstream tails change little with Re, the decay rates of the upstream tails decrease rapidly with increasing Re. This behaviour is similar to that for the relative periodic orbits in plane Poiseuille flow [38, 39]. Overall, the localization becomes weaker as Re increases.

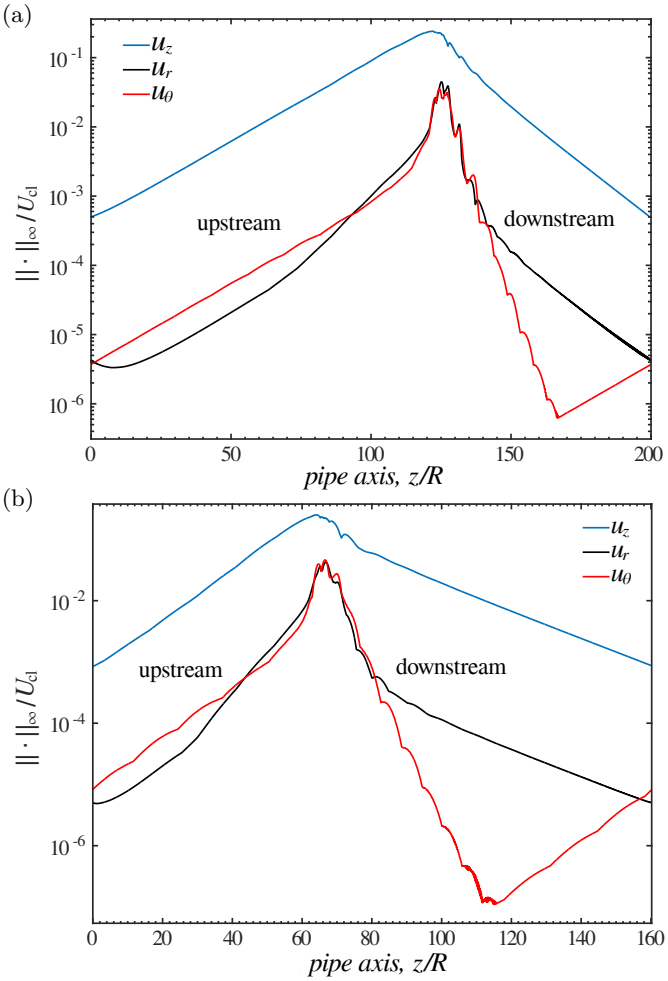

FIG. 2. Axial profiles of the infinity norm of the disturbance velocity components at $\mathrm{Re} = 3000$, (a) LB_2. (b) LB_3.

IV. LINEAR MODEL OF SPATIAL DECAY

A. Mathematical formulation of the model

The exponential decay observed at the tails suggests that these can be modelled with the linearised Navier-Stokes equations (LNSE). Following Gibson & Brand [37], we look for normal mode solutions of the form

$$\begin{aligned} \boldsymbol{u} &= \tilde{\boldsymbol{u}}(r) \exp\left[im\theta + \mu(z - ct)\right], \\ p &= \tilde{p}(r) \exp\left[im\theta + \mu(z - ct)\right], \end{aligned} \tag{4}$$

where m is the azimuthal wave number dominating at the tail, μ the spatial decay rate at the tail and c the group velocity at which the localized solution (wave packet) travels in the axial direction. The latter is not to be confused with the phase velocity of individual waves within

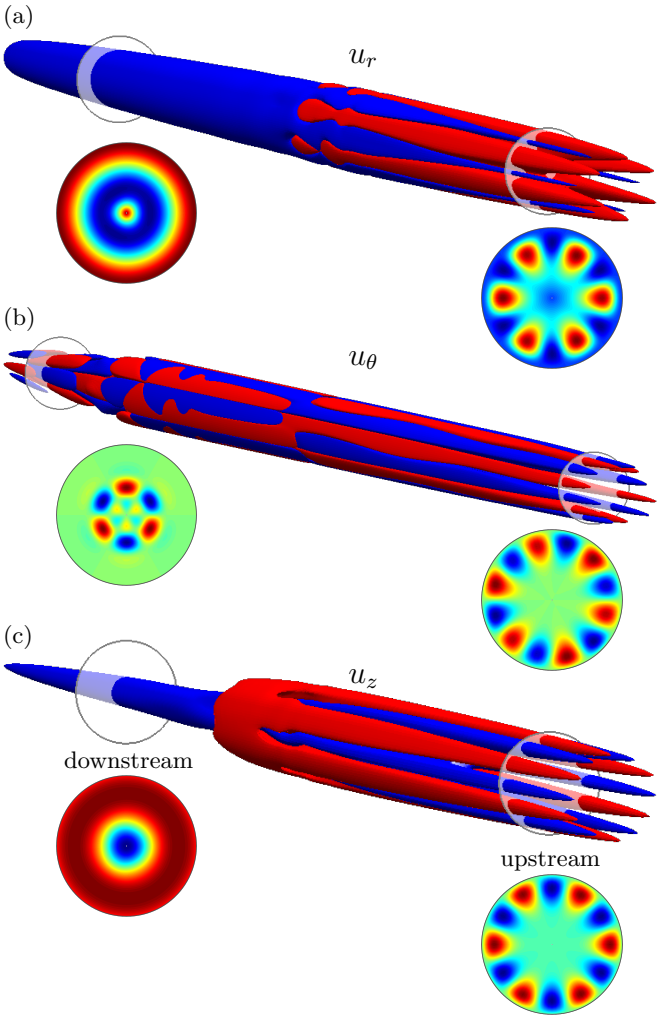

FIG. 3. Comparison of the spatial structure of the three velocity components for LB_3 at $Re = 3000$. The color coding is analogous to fig. 1 and the isovalues are given in parantheses. (a) u_r ($\pm 5 \times 10^{-5}\, U_{cl}$), (b) u_θ ($\pm 5 \times 10^{-6}\, U_{cl}$), (c) u_z ($\pm 0.015\, U_{cl}$).

the solution (envelope). Note that μ is generally complex in a spatial setting. Its real part describes the spatial attenuation (decay rate) and its imaginary part the spatial modulation of the localized solution fronts. Moreover, note that equation (4) describes the tails in a reference frame moving with the group velocity c. Although strictly speaking this equation is only valid for relative equilibria (see [39]), the temporal variation is negligible at the tails of our relative periodic orbits. Hence equation (4) is used here to model the spatial decay rates far away from their core.

Inserting ansatz (4) into the dimensionless LNSE gives:

$$-\mu c\tilde{\boldsymbol{u}} = (r^2-1)\mu\tilde{\boldsymbol{u}} + 2r\tilde{u}_r\hat{\boldsymbol{z}} - \begin{bmatrix} \partial\tilde{p}/\partial r \\ im\tilde{p}/r \\ \mu\tilde{p} \end{bmatrix} + \frac{1}{\mathrm{Re}} L\tilde{\boldsymbol{u}}$$
$$(\frac{1}{r} + \frac{\partial}{\partial r})\tilde{u}_r + \frac{im}{r}\tilde{u}_\theta + \mu\tilde{u}_z = 0, \tag{5}$$

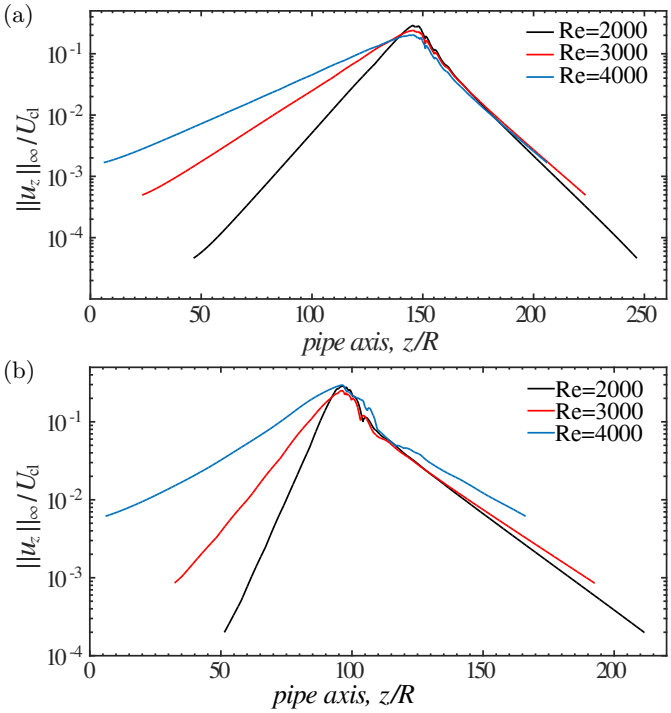

FIG. 4. Axial profiles of the infinity norm of the axial velocity disturbance for different Reynolds numbers. (a) LB_2. (b) LB_3.

where

$$L = \begin{bmatrix} \tilde{D} - \frac{1}{r^2} & -\frac{2im}{r^2} & 0 \\ \frac{2im}{r^2} & \tilde{D} - \frac{1}{r^2} & 0 \\ 0 & 0 & \tilde{D} \end{bmatrix}$$

with

$$\tilde{D} = -\frac{m^2}{r^2} + \mu^2 + \frac{1}{r}\frac{\partial}{\partial r} + \frac{\partial^2}{\partial r^2}.$$

Rearranging (5) with respect to μ one obtains the following quadratic eigenvalue problem (EVP):

$$(\mu^2 A_2 + \mu A_1 + A_0) \begin{bmatrix} \tilde{u}_r \\ \tilde{u}_\theta \\ \tilde{u}_z \\ \tilde{p} \end{bmatrix} = 0, \tag{6}$$

where

$$A_2 = \frac{1}{\mathrm{Re}} \begin{bmatrix} 1 & & & \\ & 1 & & \\ & & 1 & \\ & & & 0 \end{bmatrix},$$

$$A_1 = \begin{bmatrix} c+r^2-1 & & & \\ & c+r^2-1 & & \\ & & c+r^2-1 & -1 \\ & & 1 & 0 \end{bmatrix},$$

and

$$A_0 = \frac{1}{\mathrm{Re}} \begin{bmatrix} \tilde{D} - \frac{1}{r^2} & -\frac{2im}{r^2} & 0 & -\mathrm{Re}\frac{\partial}{\partial r} \\ \frac{2im}{r^2} & \tilde{D} - \frac{1}{r^2} & 0 & -\mathrm{Re} \cdot im/r \\ 2\mathrm{Re} \cdot r & 0 & \tilde{D} & 0 \\ \mathrm{Re}\left(\frac{1}{r} + \frac{\partial}{\partial r}\right) & \mathrm{Re} \cdot \frac{im}{r} & 0 & 0 \end{bmatrix}$$

with

$$\tilde{D} = -\frac{m^2}{r^2} + \frac{1}{r}\frac{\partial}{\partial r} + \frac{\partial^2}{\partial r^2}.$$

The radial derivatives were discretized with a spectral method at Chebyshev collocation points. In order to reduce clustering of grid points near the origin (where the solution is smoother), the differentiation matrices were computed over the interval [-1,1] using $N = 200$ points. The derivatives on (0,1] were obtained by "quotienting" out the symmetry of the 2-to-1 map from $(r-\theta)$ to (x, y) in this representation using the appropriate parities, respectively [48].

The quadratic EVP (6) can be linearized analogous to the reduction of a second-order ODE to first-order, namely by replacing it with a *linear* system with twice as many unknowns and equations [49]. Here, we choose the so-called "first companion form" (see [49]) by making the substitution $\boldsymbol{y} = \mu\boldsymbol{x} \equiv \mu[\tilde{\boldsymbol{u}}, \tilde{p}]^T$. This yields the generalized eigenvalue problem

$$\begin{bmatrix} 0 & I \\ -A_0 & -A_1 \end{bmatrix} \begin{bmatrix} \boldsymbol{x} \\ \boldsymbol{y} \end{bmatrix} = \mu \begin{bmatrix} I & 0 \\ 0 & A_2 \end{bmatrix} \begin{bmatrix} \boldsymbol{x} \\ \boldsymbol{y} \end{bmatrix}, \qquad (7)$$

which is subsequently solved with QZ-factorization (generalized Schur decomposition, see [50]). Note that we use the more descriptive label "LNSE" in the following for the solutions of equation (6)/(7).

B. Model results

For given Reynolds number Re, azimuthal wave number m and group velocity c, positive (negative) eigenvalues of EVP (6) give an approximation for the decay rate at the upstream (downstream) tail of a localized solution. The associated eigenvectors approximate the velocity profiles at the tails.

The LNSE model predictions for the tails are computed as follows. First, the Reynolds number is fixed and the group velocity c is determined from the DNS. Fig. 5 shows the evolution of c as a function of Reynolds number. Close to their saddle-node bifurcation points, LB_2 and LB_3 travel slightly faster than the mean flow speed $\overline{U} = 0.5\,U_{\mathrm{cl}}$ and the differences grow slowly as Re increases.

Second, the azimuthal wave number is determined from the velocity profiles. As shown in fig. 3, the upstream tail of LB_3 (LB_2) is dominated by a $m = 6$ ($m =$

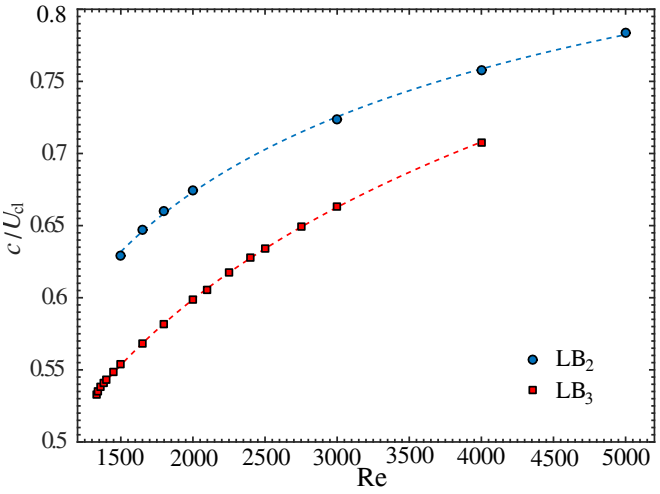

FIG. 5. Reynolds number dependence of the group velocity c with which the localized solutions LB_2 (circles) and LB_3 (squares) are advected downstream. The dashed lines are supposed to guide the eye.

4) rotational symmetry for all components, whereas their downstream tails are predominantly axisymmetric for u_r and u_z, but feature $m = 3$ ($m = 2$) in u_θ. Thus, one needs to consider both $m = 0$ and $m = 3$ ($m = 2$) separately in the model for the downstream tail. The case $m = 0$ actually decouples the azimuthal velocity from the other equations in EVP (6) leaving only the diagonal block of the matrices A_i. Since their sum is not singular, $\tilde{u}_\theta = 0$ is obtained, which is not observed (fig. 3b) but consistent with the fact that $\tilde{u}_\theta$ decays with a different rate than predicted by the axisymmetric mode for $\tilde{u}_r$ and $\tilde{u}_z$. Moreover, the mean azimuthal velocity (which is the $m = 0$ mode) has to vanish because our localized solutions are reflection symmetric, which precludes a mean rotation.

Figure 6 compares the decay rate μ of the streamwise velocity disturbance obtained by exponential fits to u_z at the tails of the solutions (square/circular markers), to the prediction based on the LNSE (dashed lines). The agreement is excellent, which confirms the validity of the model. The radial velocity profiles $\tilde{\boldsymbol{u}}(r)$ obtained from the model are compared to the DNS data in fig. 7 for LB_3. The agreement of the upstream eigenvectors (model $m = 6$) with DNS is very good. At the downstream tail, the axisymmetric ($m = 0$) model result for $\tilde{u}_r$ and $\tilde{u}_z$ match the DNS result very well, too. To obtain a model prediction for the azimuthal velocity, we solve the LNSE with $m = 3$ as suggested by fig. 3b. This yields $\Re[\mu] = -0.198R^{-1}$, whereas the decay rate obtained from DNS is $-0.266R^{-1}$. However, the magnitude of $\tilde{u}_\theta$ is very small. Note also that its decay is modulated in space (see figs. 2b, 3b) and this is correctly predicted by the model with $\Im[\mu] \neq 0$. In all other cases, the imaginary part of μ is zero, consistent with the absence of modulations in the spatial decay. The results for LB_2 are very similar to

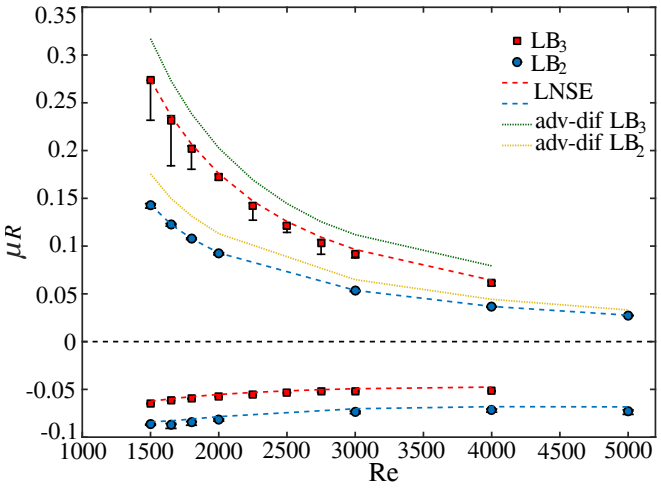

FIG. 6. Axial decay rate μ of u_z for the localized solutions as a function of Reynolds number. Circles (LB_2) and squares (LB_3) denote DNS results. The error margins have been produced by trying several axial ranges for which the respective tail was fitted. Note that except for LB_3 upstream the error is smaller than the marker size and hence barely visible. Dashed lines denote the decay rates obtained from EVP (6). The downstream fronts have $m = 0$, the upstream fronts $m = 4$ for LB_2 and $m = 6$ for LB_3. Dotted lines show the result of the advection-diffusion equation (8) for the upstream front (see IV C).

those of LB_3 and hence not shown here.

C. Contribution of terms to the spatial decay at tails

The decay rate of the streamwise tails of certain localized solutions in Couette [37] and channel [38] flows can be accurately modeled with a single equation for the streamwise velocity component of the disturbance. These authors compare the contributions of all terms of the streamwise momentum conservation equation at the solution tails, and find that three terms dominate: linear advection of the disturbance by the basic laminar flow, and diffusion of momentum in the spanwise and wall-normal directions. The model resulting from consideration of only these three terms is an advection-diffusion equation, which in pipe flow takes the following form

$$-\left(c + r^2 - 1\right)\mu\tilde{u}_z = \frac{1}{\mathrm{Re}}\tilde{D}\tilde{u}_z. \qquad (8)$$

We computed the decay rates from (8) and found that they disagree with those of the DNS and full LNSE, as also observed for spatially localized modulated Tollmien-Schlichting waves in channel flow [39]. However, the upstream rates and eigenvectors $\tilde{u}_z$ computed from the advection-diffusion model are at least comparable to the full simulation (fig. 6), whereas the downstream rates are utterly false (hence not shown in fig. 6). We assessed the

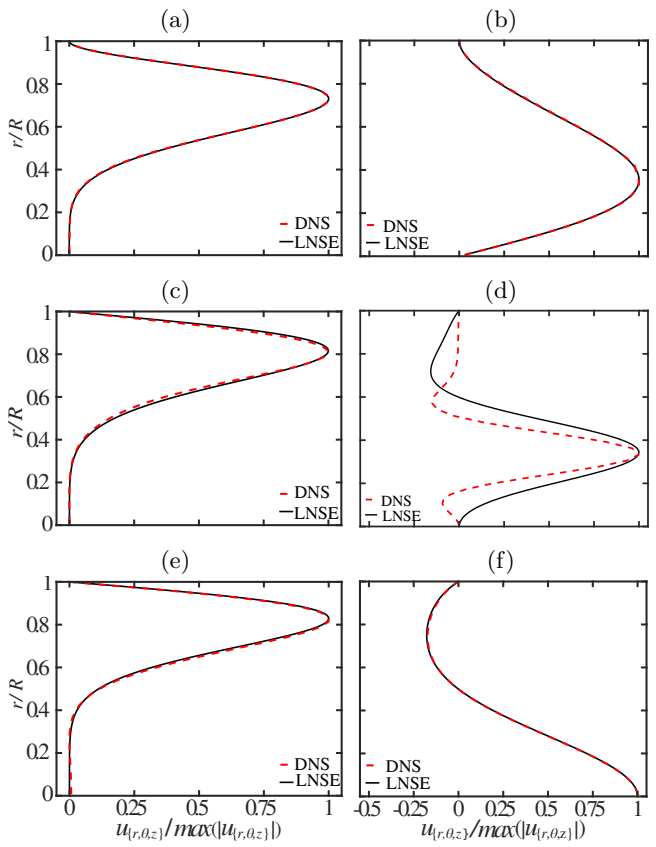

FIG. 7. Comparison of radial profiles of (a, b) u_r, (c, d) u_θ, (e, f) u_z obtained from DNS (dashed) and the LNSE (solid) for LB_3 at $\mathrm{Re} = 3000$. The left hand side profiles are located up-, the right hand ones downstream.

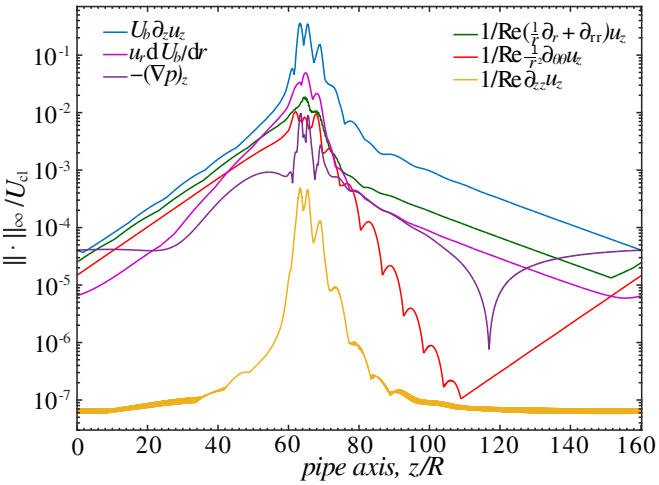

FIG. 8. Axial profiles of the infinity norm (maximum) for each individual term in the axial component of the linearized Navier-Stokes equations at $\mathrm{Re} = 3000$ for LB_3. Profiles are very similar for LB_2 and hence not shown here.

reasons underlying the failure of (8), by analyzing individual contributions of all terms in the streamwise momentum conservation equation for LB_3 (see Fig. 8, the relative contributions are similar for LB_2 and hence not shown here). The diffusive term $\frac{\partial^2}{\partial z^2}$ (yellow) is much smaller than the in-plane contributions to ∇^2 and the other terms. In fact, setting $A_2 = 0$ and solving the resulting linear eigenvalue problem does not have any effect on the decay rates, confirming that axial diffusion can be neglected. The pressure gradient (violet) in the upstream and downstream tails approaches its small and constant value in the surrounding base flow. This value is a consequence of the periodic boundary conditions and further decreases in longer pipes and with higher Re.

The relative contribution of the lift-up term $u_r \frac{\partial U_b}{\partial r}$ (magenta) was found to be larger here than for the solutions of Zammert and Eckhardt [38] in channel and of Brand and Gibson [37] in Couette flows. In our solutions, the lift-up term is of similar magnitude as the in-plane diffusion. This suggests that the absence of the lift-up term in the simple advection-diffusion model (8) is responsible for its failure. We gauged the role of the lift-up term by solving EVP (6) without it (*i.e.* the term in the first column and third row of A_0). The corresponding upstream decay rates are nearly identical to those from the advection-diffusion equation, whereas the downstream rates deviate strongly from the DNS (to a similar degree as the advection-diffusion equation).

These findings indicate that the lift-up term plays a key role in the decay of the tails of our pipe-flow solutions. For certain solutions of Couette and channel flows, the main coupling of the streamwise velocity with the other components is via the mass-conservation equation resulting in a very small wall-normal velocity, which does not influence the axial decay rate (see the vanishing value of v in the tails in fig. 2a of [38]). In pipe flow, however, one cannot neglect u_r in the tails and the radial momentum equation is strongly coupled to the axial one via $u_r \frac{\partial U_b}{\partial r}$. Hence it is not possible to formulate an accurate single-equation model for the decay of the streamwise velocity at the tails of LB_2 and LB_3, exactly as for spatially localized modulated Tollmien-Schlichting waves in channel flow [39], for which the lift-up term is also significant [51].

D. Application to a turbulent puff

Models based on LNSE have been so far applied to describe the tails of exact coherent solutions, which can be computed in symmetry subspaces only at the time of writing. Mellibovsky *et al.* [32] showed that the tails of a chaotic edge state and a turbulent puff at Re = 1900 decay exponentially, suggesting that the LNSE may correctly describe the spatial decay of such symmetrically unconstrained and hence considerably much more complex states, too. We here applied the LNSE to a turbulent puff at Re = 2000 (see fig. 9), which propagates at exactly the mean speed $c/U_{cl} = 0.5 \pm 0.00025$ [28].

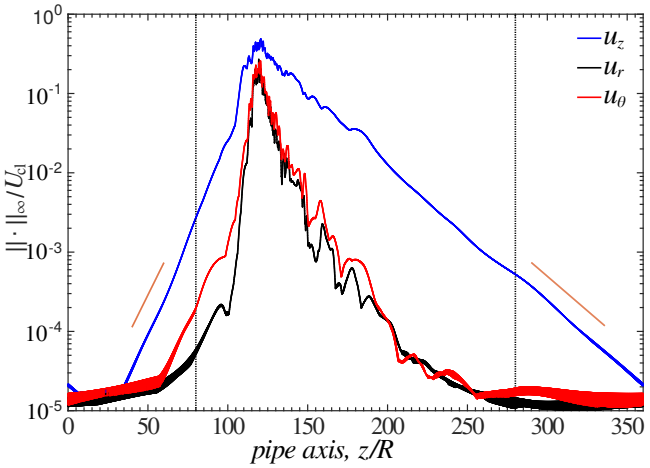

FIG. 9. Axial profiles of infinity norm of the three velocity components for a turbulent puff at Re = 2000 in a pipe of $360R$ in length. The data are from Song *et al.* [52]. The orange dashed lines show the spatial decay rates obtained from the LNSE, where $m = 1$ and $m = 0$ with $c/U_{cl} = 0.5$ were used to solve EVP (6) for the upstream and downstream tails, respectively. The dotted vertical lines indicate the locations of the velocity profiles shown in fig. 11.

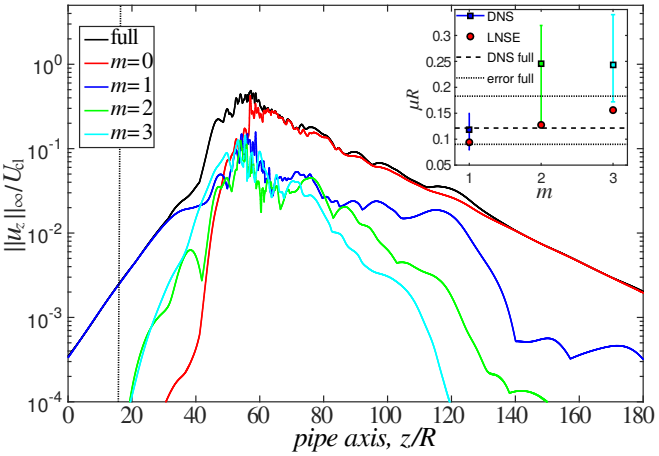

FIG. 10. Axial profiles of infinity norm of the axial velocity u_z and its first four Fourier modes for the puff in fig. 9. The black dashed line denotes the axial position of the cross-section in fig. 12. Only part of the $360R$-long pipe is shown. The inset compares the decay rates of DNS and LNSE as a function of the azimuthal mode m.

In order to decide which wave number m models the fronts of the puff best, we decomposed the velocity field into its first constituent Fourier modes. The axial profiles of these are shown in fig. 10. As in the case of the edge states, the downstream front is axisymmetric ($m = 0$), and the model gives $\mu = -0.0399R^{-1}$, which agrees very well with the slope of u_z observed in DNS (fig. 9). The downstream front presents more ambiguous results though. The profiles in fig. 10 indicate that $m = 1$ is the dominant mode with $m = 2, 3$ decaying

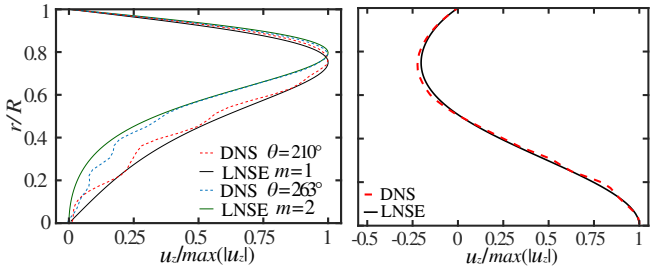

FIG. 11. Comparison of radial profiles of u_z obtained from DNS (dashed) and the LNSE model (solid) for a puff at Re = 2000. The left hand side profiles are located upstream, the right hand one downstream, the axial positions marked by dotted lines in fig. 9. In the model, $m = 0$ and $m = 1, 2$ with $c/U_{\mathrm{cl}} = 0.5$ were used to solve EVP (6) for the down- and upstream tails, respectively.

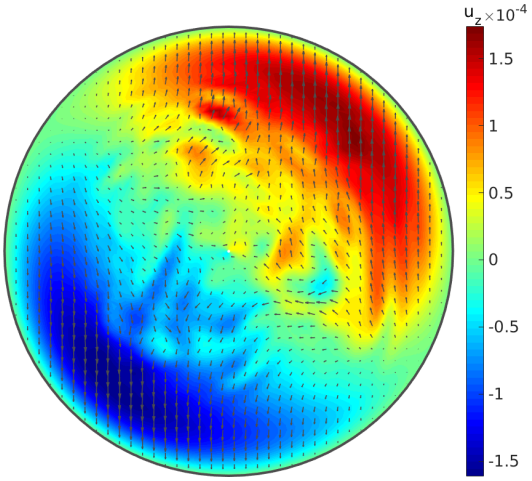

FIG. 12. Cross-section of the velocity field of the puff in fig. 9. The axial position is marked by a dashed line in fig. 10 and is the same where the upstream radial profile in fig. 11 was plotted. The in-plane components are denoted by vectors and the axial velocity by color.

twice as fast and the velocity at their tail being almost two orders of magnitude smaller. The LNSE, however, produce the closest match for $m = 2$ but the inset in fig. 10 also shows that the model decay rate computed with $m = 1$, $\mu = 0.0938R^{-1}$, is still inside the error margin of the exponential fits to the DNS profiles of both the full velocity field and the $m = 1$ Fourier mode. The model slope computed with $m = 1$ is drawn in fig. 9 with an orange dashed line and fits DNS reasonably well.

The eigenvectors of the LNSE model are compared to radial profiles of the puff in fig. 11. The agreement is excellent downstream. Upstream, both $m = 1$ and $m = 2$ match the DNS profile at different azimuthal positions, which is consistent with the above findings for the eigenvalues. Figure 12 is a look at the velocity field at the axial position of the upstream radial profile (marked by the dashed line in fig. 10). Although the velocity has no rotational symmetry, its absolute value is approximately two-fold symmetric, which might explain why the model matches DNS so well for $m = 2$.

V. DISCUSSION

Localized exact coherent structures in pipe flow exhibit exponential localization far away from their active core. This allows for accurate models of the decay based on the LNSE, as in the cases of Couette [36, 37] and channel flow [38, 39]. The solution of the resulting spatial eigenvalue problem yields two decay rates of different sign for the velocity disturbance at the upstream ($\mu > 0$) and downstream tails ($\mu < 0$), as a function of Reynolds number Re, azimuthal wave number m and group velocity c.

The localized solutions investigated here are relative periodic orbits and have either two- or three-fold rotational symmetry and are reflectional symmetric. Their upstream tails feature four/six streaks and all three components of the velocity disturbance decay at the rates as in the model for $m = 4/6$. Their downstream tails are predominantly axisymmetric and consist of large scale meridional circulation (u_r, u_z), whereas u_θ presents a two-/three-fold symmetry, is much smaller and decays at a much faster rate. The model accurately predicts the decay rates for (u_r, u_z) using $m = 0$ at the downstream tails, but the decay of u_θ is only qualitatively recovered even when $m = 2, 3$ are used in the model.

The decay rate of some solutions in Couette [37] and channel [38] flows can be accurately modeled with a single advection-diffusion equation for the streamwise velocity disturbance. Interestingly, in this equation the Reynolds number and decay rate appear only through the combination μRe, so that one may expect μ to decrease as 1/Re. However, the propagation speed of the structures was found to increase with Re in channel flow leading to a faster decrease of μ with Re upstream and a slower, nearly constant increase downstream. For spatially localized modulated Tollmien-Schlichting waves in channel flow [39], and for our solutions, a simple advection-diffusion equation cannot reproduce the results from the full LNSE. We here showed that the lift-up term $u_r \frac{\partial U_b}{\partial r}$ is significant enough so that it cannot be neglected. This term couples the radial and axial momentum equations and so it is no longer possible to retain a single equation model for the decay rate of the streamwise velocity disturbance. Despite the key role of the lift-up term, we still found that the scaling of the decay rates with Re corresponds to what one would expect from the advection-diffusion equation (8) once the dependence on c(Re) is taken into account, similar to channel flow [38, 39].

The LNSE were also applied to data from DNS of localized turbulence. Here a turbulent puff at Re = 2000 was analyzed. The spatial decay rates obtained from the model with $c/U_{\mathrm{cl}} = 0.5$, and $m = 0, 1$ for the downstream and upstream tails, were found to be in excellent agreement with the DNS data. This supports the validity

of the model for real turbulent patches and emphasizes the crucial interdependence between propagation speed of a localized structure and the spatial decay rate at its tails. Note that the dependence of μ on the group velocity c suggests that in the transition from localized puffs to expanding slugs the localization rate must change accordingly.

ACKNOWLEDGMENTS

We thank Prof. Roman Grigoriev for discussions and his critical reading of previous versions of the manuscript. Support from the Deutsche Forschungsgemeinschaft (DFG) through grant FOR 1182 and computing time from the "Regionales Rechenzentrum Erlangen (RRZE)" are acknowledged. This research was supported in part by the National Science Foundation under Grant No. NSF PHY-1125915. S. Z. acknowledges financial support by Stichting FOM/NWO-I.

[1] O. Reynolds, "On the dynamical theory of incompressible viscous fluids and the determination of the criterion," Phil. Trans. Roy. Soc. Lond. A **186**, 123–164 (1895).
[2] R. R. Kerswell, "Recent progress in understanding the transition to turbulence in a pipe," Nonlinearity **18**, R17 (2005).
[3] B. Eckhardt, T. M. Schneider, B. Hof, and J. Westerweel, "Turbulence transition in pipe flow," Ann. Rev. Fluid Mech. **39**, 447–468 (2007).
[4] B. Eckhardt, "Turbulence transition in pipe flow: some open questions," Nonlinearity **21**, T1–T11 (2008).
[5] H. Faisst and B. Eckhardt, "Traveling waves in pipe flow," Phys. Rev. Lett. **91**, 224502 (2003).
[6] H. Wedin and R. R. Kerswell, "Exact coherent structures in pipe flow: travelling wave solutions," J. Fluid Mech. **508**, 333–371 (2004).
[7] Y. Duguet, C. C. T. Pringle, and R. R. Kerswell, "Relative periodic orbits in transitional pipe flow," Phys. Fluids **20**, 114102 (2008).
[8] A. P. Willis, P. Cvitanović, and M. Avila, "Revealing the state space of turbulent pipe flow by symmetry reduction," J. Fluid Mech. **721**, 514–540 (2013).
[9] J. F. Gibson, J. Halcrow, and P. Cvitanović, "Visualizing the geometry of state space in plane Couette flow," J. Fluid Mech. **611**, 107–130 (2008).
[10] G. Kawahara, M. Uhlmann, and L. van Veen, "The significance of simple invariant solutions in turbulent flows," Ann. Rev. Fluid Mech. **44**, 203–225 (2012).
[11] T. M. Schneider, B. Eckhardt, and J. Vollmer, "Statistical analysis of coherent structures in transitional pipe flow," Phys. Rev. E **75**, 066313 (2007).
[12] B. Suri, J. Tithof, R. O. Grigoriev, and M. F. Schatz, "Forecasting fluid flows using the geometry of turbulence," Phys. Rev. Lett. **118**, 114501 (2017).
[13] P. Cvitanović, "Invariant measurement of strange sets in terms of cycles," Phys. Rev. Lett. **61**, 2729–2732 (1988).
[14] P. Cvitanović and B. Eckhardt, "Periodic-orbit quantization of chaotic systems," Phys. Rev. Lett. **63**, 823–826 (1989).
[15] P. Cvitanovic and B. Eckhardt, "Periodic orbit expansions for classical smooth flows," J. Phys. A **24**, L237 (1991).
[16] P. Cvitanović, "Recurrent flows: The clockwork behind turbulence," J. Fluid Mech. **726**, 1–4 (2013).
[17] T. Kreilos and B. Eckhardt, "Periodic orbits near onset of chaos in plane Couette flow," Chaos **22**, 047505 (2012).
[18] A. P. Willis, K. Y. Short, and P. Cvitanović, "Symmetry reduction in high dimensions, illustrated in a turbulent pipe," Phys. Rev. E **93**, 022204 (2016).
[19] O. Reynolds, "An experimental investigation of the circumstances which determine whether the motion of water shall be direct or sinuous, and of the law of resistance in parallel channels," Phil. Trans. Roy. Soc. Lond. **35**, 84–99 (1883).
[20] H. W. Emmons, "The laminar-turbulent transition in a boundary layer," J. Aero. Sci. **18**, 490 (1951).
[21] N. Tillmark and H. P. Alfredsson, "Experiments on transition in plane Couette flow," J. Fluid Mech. **235**, 89–102 (1992).
[22] G. Lemoult, J.-L. Aider, and J. E. Wesfreid, "Turbulent spots in a channel: large-scale flow and self-sustainability," J. Fluid Mech. **731**, R1 (2013).
[23] I. J. Wygnanski and F. H. Champagne, "On transition in a pipe. Part 1. The origin of puffs and slugs and the flow in a turbulent slug," J. Fluid Mech. **59**, 281–335 (1973).
[24] Dwight Barkley, Baofang Song, Vasudevan Mukund, G. Lemoult, M. Avila, and B. Hof, "The rise of fully turbulent flow," Nature **526**, 550–553 (2015).
[25] R. T. Cerbus, C.-C. Liu, G. Gioia, and P. Chakraborty, "Kolmogorovian turbulence in transitional pipe flows," (2017), arXiv:1701.04048 [physics.flu-dyn].
[26] J. C. Rotta, "Experimenteller Beitrag zur Entstehung turbulenter Strömung im Rohr," Arch. Appl. Mech. **24**, 258–281 (1956).
[27] D. Moxey and D. Barkley, "Distinct large-scale turbulent-laminar states in transitional pipe flow," Proc. Natl. Acad. Sci. USA **107**, 8091 (2010).
[28] K. Avila, D. Moxey, A. de Lozar, M. Avila, D. Barkley, and B. Hof, "The onset of turbulence in pipe flow," Science **333**, 192–196 (2011).
[29] T. M. Schneider, D. Marinc, and B. Eckhardt, "Localized edge states nucleate turbulence in extended plane Couette cells," J. Fluid Mech. **646**, 441–451 (2010).
[30] M. Avila, F. Mellibovsky, N. Roland, and B. Hof, "Streamwise-localized solutions at the onset of turbulence in pipe flow," Phys. Rev. Lett. **110**, 224502 (2013).
[31] P. Ritter, F. Mellibovsky, and M. Avila, "Emergence of spatio-temporal dynamics from exact coherent solutions in pipe flow," New J. Phys. **18**, 083031 (2016).
[32] F. Mellibovsky, A. Meseguer, T. M. Schneider, and B. Eckhardt, "Transition in localized pipe flow turbulence," Phys. Rev. Lett. **103**, 054502 (2009).
[33] T. Kreilos, B. Eckhardt, and T. M. Schneider, "Increasing lifetimes and the growing saddles of shear flow tur-

bulence," Phys. Rev. Lett. **112**, 044503 (2014).
[34] S. Zammert and B. Eckhardt, "Crisis bifurcations in plane Poiseuille flow," Phys. Rev. E **91**, 041003 (2015).
[35] S. Zammert and B. Eckhardt, "Streamwise and doubly-localised periodic orbits in plane Poiseuille flow," J. Fluid Mech. **761**, 348–359 (2014).
[36] J. F. Gibson and E. Brand, "Spanwise-localized solutions of planar shear flows," J. Fluid Mech. **745**, 25–61 (2014).
[37] E. Brand and J. F. Gibson, "A doubly localized equilibrium solution of plane Couette flow," J. Fluid Mech. **750**, R3 (2014).
[38] S. Zammert and B. Eckhardt, "Streamwise decay of localized states in channel flow," Phys. Rev. E **94**, 041101 (2016).
[39] J. Barnett, D. R. Gurevich, and R. O. Grigoriev, "Streamwise localization of traveling wave solutions in channel flow," (2016), arXiv:1609.06608 [nlin.PS].
[40] M. Chantry, A. P. Willis, and R. R. Kerswell, "Genesis of streamwise-localized solutions from globally periodic traveling waves in pipe flow," Phys. Rev. Lett. **112**, 164501 (2014).
[41] A. P. Willis, *The openpipeflow.org Navier-Stokes solver*, Tech. Rep. (2016).
[42] D. Rempfer, "On boundary conditions for incompressible navier-stokes problems," Appl. Mech. Rev. **59**, 107–125 (2006).
[43] A. Guseva, A. P. Willis, and M. Avila, "Transition to magnetorotational turbulence in Taylor-Couette flow with imposed azimuthal magnetic field," New J. Phys. **17**, 093018 (2016).
[44] T. Itano and S. Toh, "The dynamics of bursting process in wall turbulence," J. Phys. Soc. Jpn. **70**, 703–716 (2001).
[45] J. D. Skufca, J. A. Yorke, and B. Eckhardt, "Edge of chaos in a parallel shear flow," Phys. Rev. Lett. **96**, 174101 (2006).
[46] D. Viswanath, "Recurrent motions in plane Couette flow," J. Fluid Mech. **580**, 339–358 (2007).
[47] C. C. T. Pringle, A. P. Willis, and R. R. Kerswell, "Minimal seeds for shear flow turbulence: using nonlinear transient growth to touch the edge of chaos," J. Fluid Mech. **702**, 415–443 (2012).
[48] L. N. Trefethen, *Spectral Methods in Matlab* (Society for Industrial and Applied Mathematics, Philadelphia, PA, USA, 2000).
[49] F. Tisseur and K. Meerbergen, "The quadratic eigenvalue problem," SIAM Rev. **43**, 235–286 (2001).
[50] C. B. Moler and G. W. Stewart, "An Algorithm for Generalized Matrix Eigenvalue Problems," SIAM J. Num. Anal. **10**, 241–256 (1973).
[51] R. O. Grigoriev, private communication.
[52] B. Song, D. Barkley, B. Hof, and M. Avila, "Speed and structure of turbulent fronts in pipe flow," J. Fluid Mech. **813**, 1045–1059 (2017).